

Bridge–Pier Caisson foundations subjected to normal and thrust faulting: physical experiments versus numerical analysis

G. Gazetas · O. Zarzouras · V. Drosos · I. Anastasopoulos

Received: 29 October 2013 / Accepted: 20 June 2014 / Published online: 7 August 2014
© Springer Science+Business Media Dordrecht 2014

Abstract Surface fault ruptures can inflict serious damage to engineering structures built on or near them. In the earthquakes of Kocaeli, Chi-chi, and Wenchuan a number of bridges were crossed by the emerging normal or thrust faults suffering various degrees of damage. While piles have proved incapable of tolerating large displacements, massive embedded caisson foundations can be advantageous thanks to their rigidity. The paper explores the key mechanisms affecting the response of such bridge foundations subjected to dip-slip (normal or thrust) faulting. A series of physical model experiments are conducted in the National Technical University of Athens, to gain a deeper insight in the mechanics of the problem. The position of the caisson relative to the fault rupture is parametrically investigated. High-resolution images of the deformed physical model is PIV-processed to

compute caisson displacements and soil deformation. A novel laser scanning technique, applied after each dislocation increment, reveals the surface topography (the relief) of the deformed ground. 3D finite element analyses accounting for soil strain-softening give results in accord with the physical model tests. It is shown that the caisson offers a kinematic constraint, diverting the fault rupture towards one or both of its sides. Depending on the caisson's exact location relative to the rupture, various interesting interaction mechanisms develop, including bifurcation of the rupture path and diffusion of plastic deformation.

Keywords Fault-rupture apparatus · Finite elements · Embedded foundation · Soil–structure interaction · Bifurcation · Shear band

G. Gazetas (✉)
School of Civil Engineering, National Technical
University of Athens, Athens, Greece
e-mail: gazetas@ath.forthnet.gr; gazetas@central.ntua.gr

O. Zarzouras
Fugro Geoconsulting, Brussels, Belgium

V. Drosos
University of California Berkeley, Berkeley, CA, USA
e-mail: vadrosos@gmail.com

I. Anastasopoulos
University of Dundee, Dundee, UK
e-mail: i.anastasopoulos@dundee.ac.uk

1 Introduction

In large magnitude earthquakes the seismogenic fault may rupture all the way to the ground surface, creating a (tectonic) hazard that is different in nature than the (dynamic) threat of ground shaking. Manifesting itself most frequently in the form of a scarp or of a trace on the ground, the fault rupture emerges slowly (in tens of minutes) and is profoundly affected by the presence of deep soil deposits overlying the basement rock. Propagation of the rupture in the soil deposit modifies the direction of its path and tends to ameliorate the

steep ground scarp once the rupture outcrops. Structures straddling the fault are threatened by structural damage (the extreme being collapse) and excessive movements (most significant: uncontrollable rotation). Such effects on structures have been numerous and conspicuous in the earthquakes of Nicaragua 1972, Kocaeli 1999, Düzce 1999, Chi-Chi 1999, Wenchuan 2008 [1–10].

Yet, in a number of cases, structures survived major fault offsets with hardly any damage. Apparently, the interplay of the propagating in the soil fault rupture (the moving “shear band”) with the foundation-structure system plays a critical role in the overall structural performance. Several studies have been published in recent years exploring the consequences of such interaction [1, 11–15]. One of the most important general conclusions of these studies is that, depending on their rigidity, continuity, and surcharge loading, foundations can often force the fault rupture to deviate and thus they protect the structure from the imposed fault deformation. Several strategies to protect a facility from the danger of a fault rupturing directly underneath it have been proposed in the literature [16–18]. A set of practical design recommendations has also been formulated in Gazetas et al. [19] while, more recently, research into the mechanics of fault-rupture–soil–foundation–structure interaction (FR-SFSI) has revealed a potentially favourable role of massive caissons in comparison with shallow and piled foundations.

The research presented herein involves both experimental testing and 3D numerical exploration of the mechanisms of dip-slip FR-SFSI with caisson foundations. A series of reduced-scale (1/20) physical model tests were conducted in the Laboratory of Soil Mechanics of the National Technical University of Athens to investigate the response of a square in plan caisson foundation of prototype dimensions $5\text{ m} \times 5\text{ m} \times 10\text{ m}$, founded on a 15 m thick layer of dry dense sand. The focus is on the influence of:

- the caisson’s position relative to the fault rupture
- the fault type (normal or reverse), and
- the fault offset.

The experiments are numerically simulated with finite elements; validation of the analysis enables a more detailed theoretical parametric study which could offer additional insights.

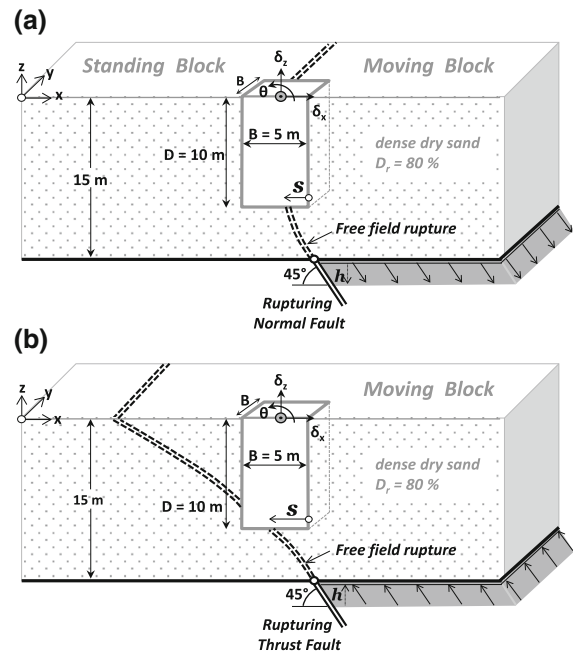


Fig. 1 Sketch of the studied problem indicating the basic parameters and dimensions at prototype scale, for the cases of **a** a normal, and **b** a thrust rupturing fault

2 Physical modelling

As sketched in Fig. 1, the investigated problem refers to a square in plan reinforced concrete (RC) caisson foundation of prototype dimensions $10 \times 5 \times 5\text{ m}$ ($H \times W \times D$), fully embedded in a 15 m deep dense sand stratum. The relative density D_r of the soil stratum is approximately 80 % and the dead load of the caisson foundation is 20 MN.

As discussed in [13] and [15], the selected caisson dimensions are typical for a highway bridge pier carrying a 1,200 mg deck load. The bedrock is subjected to tectonic dislocation due to a 45° “dip-slip” fault (normal or reverse) having a vertical offset component h . The position where the fault would cross the base of the caisson, s , if the rupture propagation were unperturbed by the presence of the caisson, is shown in the figure. The displacements and rotation of the caisson (Δ_x , Δ_z , and θ) along with the displacements in the soil mass are recorded during the evolution of the phenomenon, both in the experimental and the numerical simulation.

A total of 5 physical model tests (2 for normal and 3 for reverse faulting) are conducted in the fault rupture

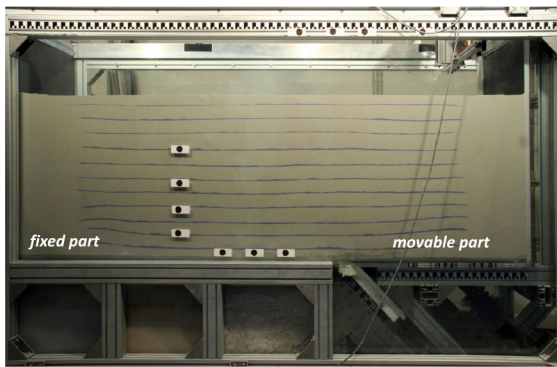


Fig. 2 Photo of the fault rupture box (FRB) used for the experiments filled with soil (free-field case)

box (FRB) of the Laboratory of Soil Mechanics. Besides the style of faulting and the magnitude of offset, the experiments aim at investigating the effect of the position of the caisson foundation relative to the outcropping fault rupture. Before studying the interaction between caisson and fault rupture, the free field problem must be simulated (for both normal and reverse faulting) in order to define the position of the foundation relative to the fault rupture, via parameter s .

The physical model experiments are conducted utilizing a custom built FRB, a split-box (Fig. 2) designed to simulate the propagation of fault rupture through soil and its interaction with foundation–structure systems. The apparatus is equipped with a fixed and a movable part, which moving up or down simulates normal or reverse faulting. At the two sides of the split box, special transparent barriers are installed to allow observation of soil deformations. With internal dimensions $2.6 \times 1.1 \times 1.0$ m (length \times width \times height), the apparatus is capable of simulating soil deposits of up to 1 m in height, at a maximum imposed fault offset of ± 0.2 m (i.e., offset–over–thickness ratio of 20 %). Along the two long sides of the box transparent barriers are installed, composed of a Plexiglas sheet from the outside for rigidity and durability, and a glass sheet from the inside for scratch protection and friction minimization. These transparent “windows” are used to record the evolution of soil deformation during the test.

Cole and Lade [20] were among the first to use a split box to simulate fault rupture propagation through granular soil, in a series of small scale free field rupture tests. Similar split containers have been used to investigate the behaviour of buried pipelines

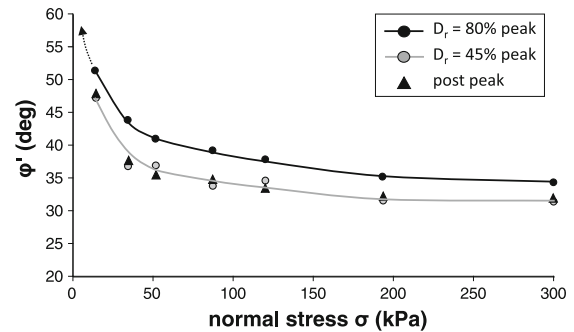


Fig. 3 Direct shear test results for the Longstone sand used in the tests: mobilized friction angle as a function of stress level

subjected to strike-slip faulting [21–23]. Taking account of the capacity of the NTUA-FRB, a model scale of 1:20 was selected, appropriate for the reduced-scale physical modeling of the prototype problem. The dimensions and material properties were scaled down employing appropriate similarity laws [e.g. 24]. The two out-of-plane boundaries of the FRB (i.e., the two “windows”) are considered to act as symmetry planes, and hence only half of the caisson foundation is modelled [see also 15]. This allows simultaneous testing of two different cases per experiment (e.g., free field on the one side and a caisson foundation at the other side, or two caissons positioned at different locations).

2.1 Soil properties

The backfill consists of dry “Longstone” sand, a very fine uniform quartz sand with $d_{50} = 0.15$ mm and uniformity coefficient $C_u = D_{60}/D_{10} \approx 1.4$, industrially produced with adequate quality control. The void ratios at the loosest and densest state were measured as $e_{max} = 0.995$ and $e_{min} = 0.614$, while $G_s = 2.64$. Direct shear tests have been carried out to obtain the peak and post-peak strength characteristics of the sand. Medium loose [$D_r = (45 \pm 2\%)$] and dense [$D_r = (80 \pm 3\%)$] sand specimens were tested at normal stresses ranging from 13 kPa (due to the weight of the top cap only) to 300 kPa. As shown in Fig. 3 and documented in [25], the angle of shearing resistance depends strongly on the stress level; for stresses higher than 120 kPa $\phi' \approx 32^\circ$ while for lower stresses ϕ' increases up to 55° . For the dense specimens the angle of shearing resistance $\approx 35^\circ$ for the higher stress levels and $\approx 51^\circ$ at the lowest normal stress tested. These values drop after

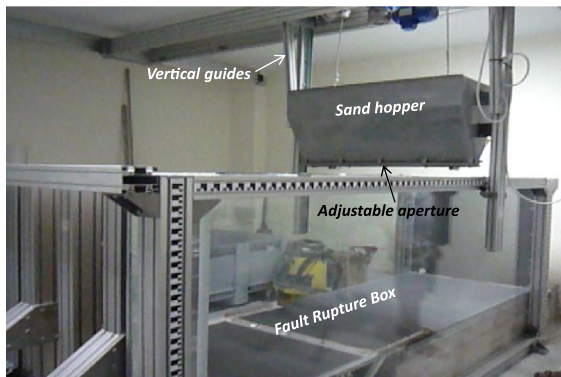


Fig. 4 Custom-built automated sand-raining system used for preparation of the physical models

displacement of 6 mm to post-peak critical-state. The angle of dilation depends on the effective stress [26], with a maximum value $\psi \approx 12^\circ$.

To realistically simulate the concrete–soil interface, the side surfaces of the caisson are covered with sandpaper of similar friction angle with the sand.

2.2 Model preparation and instrumentation

The model is prepared by a custom-built automated sand raining system (Fig. 4). The latter consists of a sand hopper hanged from a beam, which travels back and forth at an electrically-controllable speed. The vertical position of the sand hopper is also electrically adjusted, sliding along two vertical support beams. The remotely controlled movement of the sand hopper determines the pluviation speed and height of drop. The resulting sand density depends on the raining height and the sand discharge rate. The height is controlled by the vertical position of the hopper; the discharge rate by the aperture of the hopper and the pluviation speed. The raining system has been calibrated for the “Longstone” sand used in our experiments, as described in [25].

The sand is rained in layers ≈ 5.5 cm thick. At the end of each layer, a strip of painted sand is added to allow direct identification of fault rupture propagation path in the soil, and facilitate image analysis. For the free field simulation, the procedure is repeated until the total height of 75 cm, which corresponds to a prototype dense sand deposit of 15 m depth. For the models containing a caisson foundation, the sand raining is performed as previously described, until reaching 25 cm from the bedrock (i.e., 5 m in prototype scale). This is the foundation level of the base of the caisson foundation.

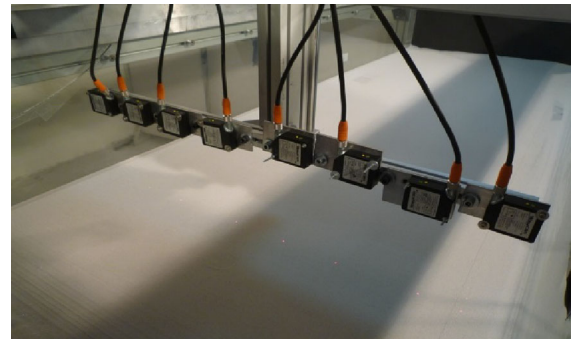


Fig. 5 Laser scanning of the surface of the physical model using a moving (at constant speed) row of laser displacement transducers

The caisson is carefully placed in its position utilizing a manual crane, with special care on avoiding disturbance of the soil under the caisson. After installation of the caisson foundation, the sand raining is resumed, and goes on until reaching the total height of 75 cm.

While conducting the test, the bedrock displacement is imposed very slowly in small consecutive increments, each of the order of 2 mm. After each displacement increment, a high-resolution digital camera photographed the deformed physical model. The digital images, subsequently analysed with the Geo-PIV software [27], give the caisson displacements and shear strains in the soil. In addition to the above, after each displacement increment the ground surface was scanned from above using a custom-built system (Fig. 5), consisting of a moving row of 8 laser displacement transducers, placed perpendicularly to the axis of the model. The row moves horizontally from one end of the container to the other at constant speed, scanning the ground surface to produce its new relief for each increment of fault dislocation h .

3 Numerical simulation

The finite element (FE) method has been applied successfully by several researchers to simulate the fault rupture as it propagates through soil in the free field and as it interacts with foundation–structure systems [14, 15, 28–30]. In this study, the soil–foundation system is analysed in 3D. The FE model (Fig. 6) is a numerical replica of the FRB, and hence its dimensions are equal to those of the split-box. Converted to prototype scale the depth of the soil

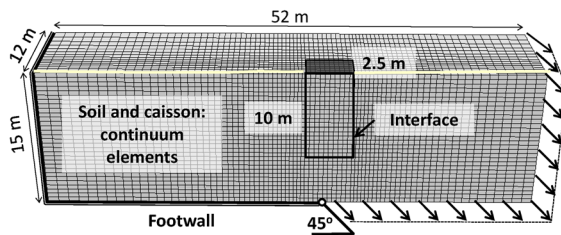


Fig. 6 3D FE discretization, along with key model dimensions and boundary conditions

stratum is 15 m, while the length and width of the soil are 52 and 12 m, respectively. But since the experiment is at reduced scale, such a representation cannot be realistic unless scale effects are taken carefully into account. To this end, we introduce the variability of soil properties with normal stress level. Taking advantage of problem symmetry, only half of the model is analyzed. The geometry of the model fulfils the requirement of a length/depth ratio >4 , suggested by [11], in order to avoid parasitic boundary effects.

Soil and caisson are simulated with 8-noded hexahedral continuum elements. At the central part of the model, where strain localization is expected, the mesh is finer (element size $d_{FE} = 0.4$ m). The bottom boundary is split in two; one part remains stationary (footwall, left), and the other (moving block, right) moves up or down to simulate normal or reverse faulting, respectively. After imposing the geostatic stresses and the dead load of the caisson foundation, the fault dislocation is applied in small quasi-static analysis increments.

The soil is modelled employing the elastoplastic constitutive model described in [29], encoded as an ABAQUS user subroutine. The model incorporates elastic pre-yielding soil behaviour, assuming a shear modulus G_s linearly increasing with depth. A Mohr–Coulomb failure criterion is combined with isotropic strain softening, reducing the friction φ and dilation ψ angles with octahedral plastic shear strain γ_{oct}^{pl} according to the following relationships:

$$[\varphi; \psi] = \begin{cases} \varphi_p - \frac{\varphi_p - \varphi_{cs}}{\gamma_f^{pl}} \gamma_{oct}^{pl}; \psi_p \left(1 - \frac{\gamma_{oct}^{pl}}{\gamma_f^{pl}}\right), & \text{for } 0 \leq \gamma_{oct}^{pl} < \gamma_f^{pl} \\ \varphi_{cs}; 0 & \text{for } \gamma_{oct}^{pl} \geq \gamma_f^{pl} \end{cases} \quad (1)$$

where φ_p and φ_{cs} the peak and critical-state soil friction angles; ψ_p the peak dilation angle; and γ_f^{pl} the octahedral plastic shear strain at the end of softening. Constitutive soil parameters are calibrated on the basis of direct shear tests, and the model has been validated with centrifuge experiments conducted at the University of Dundee, as discussed in detail in [29].

For the small stresses of the reduced-scale experiments presented herein, the mobilized friction angle depends strongly on the stress level: scale effects. This problem does not exist in centrifuge model tests, where the stress level is equivalent to the prototype thanks to the centrifugal acceleration which multiplies the gravitational force by a factor of N (i.e., equal to the scale of the model). To overcome this problem, the octahedral stress level is taken into account with φ and ψ being iteratively adjusted (according to Eq. 1) to be consistent with γ_f^{pl} and σ_{oct} . For this purpose, the experimental results of Fig. 3 are used directly, applying a simple curve-fitting rule. Thus, the analysis is roughly equivalent to the stress conditions of the experiments.

The caisson foundation is of course linearly elastic. The soil–foundation interface is modelled using special contact elements that allow sliding, uplifting and/or separation (loss of contact). In the experiments, sandpaper was glued on the model caisson to increase the interface friction to realistic levels. Thus, a coefficient of friction $\mu = 0.7$ is used appropriately for the interface between the sand and the sandpaper.

4 Normal faulting

The experimental results are discussed in parallel with those obtained through numerical analysis. The free field case is presented first, followed by the interaction of the caisson foundation with the outcropping fault rupture, for two different characteristic locations. The results are presented and discussed in terms of:

Fig. 7 Normal fault rupture propagation in the free field. Comparison of **a** images of the deformed physical model, compared to **b** 3-D FE analysis deformed mesh with superimposed plastic deformation

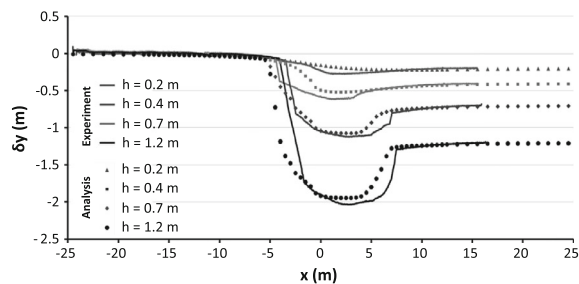
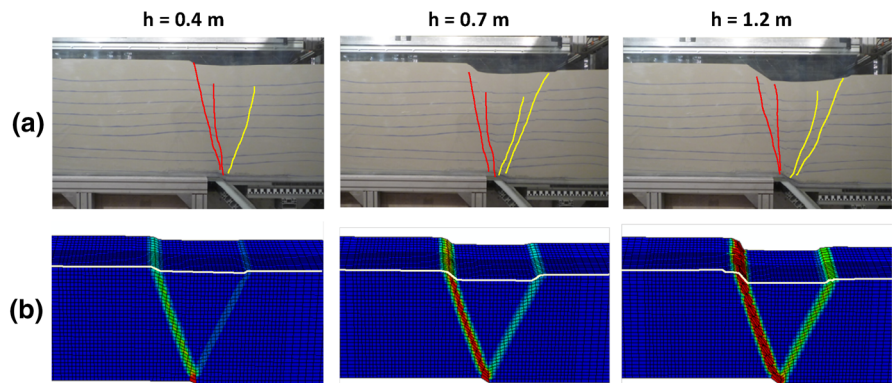


Fig. 8 Normal fault rupture propagation in the free field. Comparison between numerical analysis and experiment in terms of vertical displacement profile at the ground surface for different characteristic values of imposed offset h

(a) deformations and strain localization within the soil, revealing the key interaction mechanisms; (b) surface displacement profiles; and (c) foundation translation and rotation. In all presented cases the zero point of the horizontal, x , axis corresponds to the location of fault initiation at bedrock level.

4.1 Free-field fault rupture propagation

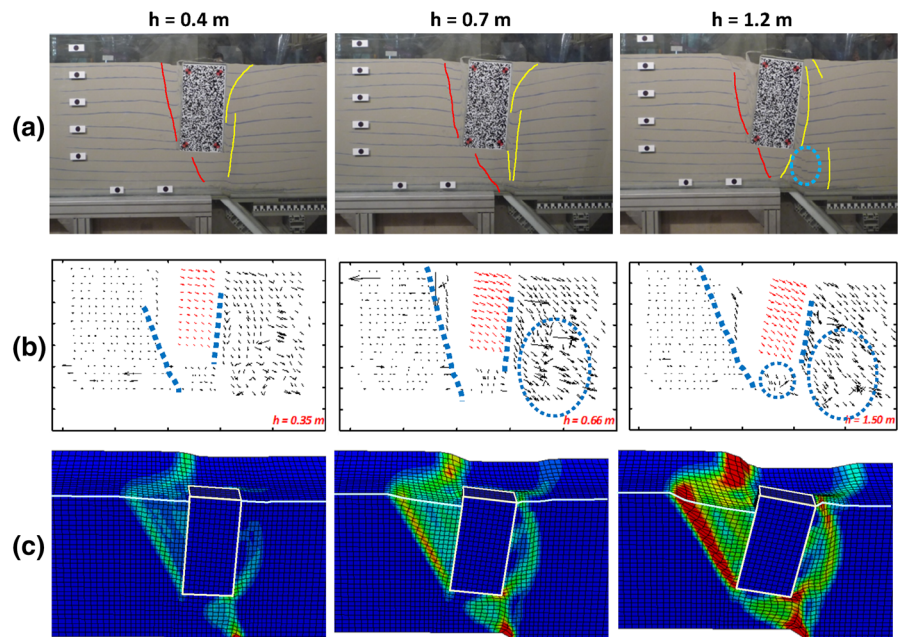
In Fig. 7 images of the deformed physical model are compared with FE deformed mesh on which plastic strain contours are superimposed. Figure 8 compares numerical and experimental results in terms of vertical displacement profile of the ground surface for four values of h . Evidently, the primary fault rupture reaches the ground surface just after 0.3 m of imposed bedrock offset h . Due to the large density of the sand combined with the aforementioned scale effects the rupture path is quite steep, reaching the surface at -3 m: an effective dip angle of roughly 78° . At the same time, a secondary antithetic rupture has already

made its appearance, having propagated almost 80 % of the distance to the ground surface. The latter is due to the extension caused by the 45° dip of the fault at bedrock. The analysis predicts a slightly less steep rupture path, but nevertheless agrees generally well with the experiment.

In the experiment, the increase of the imposed fault offset to $h = 0.7$ m leads to the development of another set of primary and secondary ruptures, both propagating more steeply (Fig. 7). Also, the vertical displacement profiles of Fig. 8 show that the primary fault scarp progressively moves towards the footwall (leftward), and the secondary one towards the moving block (rightward). As a result, the fault graben that is formed between the two ruptures (primary and secondary) progressively becomes wider. This very interesting response is believed to be directly related to scale effects. At the beginning, the sand mobilizes its very large friction angle (of the order of 60°), leading to the very steep initial rupture path. With the accumulation of deformation, the sand within the shear band starts softening and the mobilized friction angle is reduced to the residual value (of the order of 32°), rendering the initial rupture paths kinematically inadmissible. At the same time, due to the imposed extensional deformation, the sand in the vicinity of the initial rupture has loosened, and its mobilized friction angle has become much lower (corresponding to loose rather than dense sand). For this reason, the newly developing ruptures are less steep than the initial ones. The numerical analysis cannot possibly capture such complicated soil response in full detail, but it does predict the final rupture paths fairly accurately.

Further increase of the imposed deformation to $h = 1.2$ m does not lead to any appreciable change,

Fig. 9 Interaction of the caisson foundation with a normal fault rupture at $s/B = -0.16$. Comparison of experimental with numerical analysis results **a** images of the deformed physical model, and **b** displacement vectors computed through image analysis, compared to **c** 3D FE deformed mesh with superimposed plastic strain contours



with the plastic deformation accumulating along the already developed rupture paths. The experimental results are in good agreement with previous smaller-scale experiments [e.g. 20] and centrifuge model tests [15, 31], but they also compare qualitatively well with field observations [28]. In general, normal faults tend to refract at the soil–bedrock interface, becoming steeper. However, this inherent tendency is further amplified due to scale effects. This is confirmed by the analysis, which could not predict the experimental rupture path, unless scale effects were properly accounted for. The same model has been successful in predicting centrifuge model test results [29]. Hence the difference is attributable to scale effects.

4.2 Interaction of the Caisson with a normal fault

4.2.1 $s/B = 0.16$

In this test the caisson was positioned so that the unperturbed (free-field) rupture would have crossed its base in the vicinity of its right corner. Experimental images and displacement vectors computed through image analysis are compared with FE deformed mesh with plastic strain contours in Fig. 9. Evidently, the caisson acts as a kinematic constraint, substantially altering the rupture path. For $h = 0.4$ m of bedrock fault offset, the primary rupture deviates towards the

footwall (i.e., to the left) and a secondary rupture path develops towards the moving block, “grazing” the right wall of the caisson foundation (Fig. 9a). Close to the ground surface, and to the right of the caisson (i.e., in the moving block), another rupture is observed. The latter is associated with active conditions, as the block moves outwards and downwards. At the same time, the soil underneath the caisson is extensively disturbed, and sliding at the soil–caisson interface is taking place.

For $h = 0.7$ m the caisson rotates towards the moving block, and the rupture to the left of the caisson constitutes the prevailing mechanism. Further increase of h to 1.2 m leads to a complex combination of shearing mechanisms, as the soil to the right of the caisson is subjected to extension due to the main faulting mechanism, but also to compression at the top due to the increasing rotation of the foundation. At this stage of deformation, there seems to have been a technical problem with the image analysis; its results close to the bottom of the model (Fig. 9b) are thus deemed unreliable.

Overall, the numerical results (Fig. 9c) are in reasonable accord with the experiment, predicting similar deformation mechanisms and rupture paths. Moreover, the analysis predicts substantial loss of contact between the soil and the caisson near the footwall (i.e., to the left), which is in agreement with

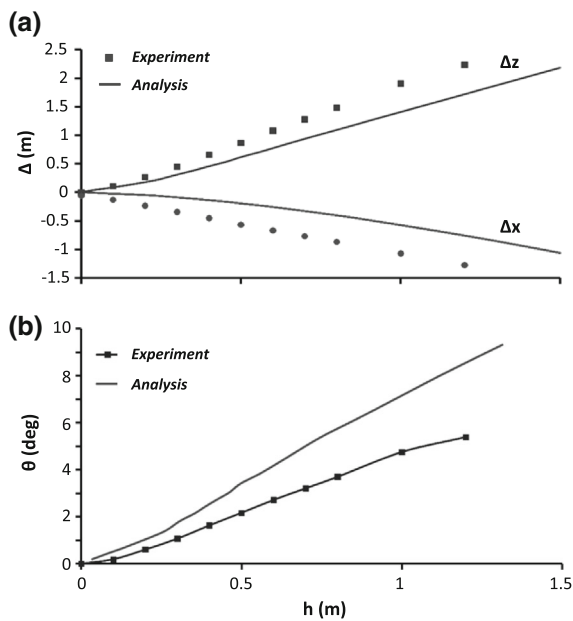


Fig. 10 Interaction of the caisson foundation with a normal fault rupture at $s/B = -0.16$. Comparison of experimental with numerical analysis results in terms of evolution with bedrock offset h of **a** vertical Δz and horizontal Δx displacement, and **b** rotation θ at the top of the caisson foundation

the experimental observations. However, the extent of this gap is underestimated in the analysis. Despite the aforementioned discrepancies, the numerical analysis predicts translational and rotational movement of the caisson quite successfully as shown in Fig. 10. The analysis slightly underestimates the vertical Δz and horizontal Δx displacement at the top of the caisson, but overestimates its rotation θ .

4.2.2 $s/B = 0.80$

In this test, the caisson foundation is placed in such a manner that the unperturbed fault rupture would have crossed near its left edge. Selected images and displacement vectors computed through image analysis are compared with FE deformed mesh and its plastic strain contours in Fig. 11.

For $h = 0.4$ m, the primary fault rupture has already developed, initiating from the bedrock dislocation point, interacting with the left edge of the caisson base, being slightly diverted towards the footwall, and finally becoming steeper as it propagates to the ground surface (Fig. 11a). The corresponding incremental displacement plot confirms the diversion

of the fault rupture to the left of the caisson base. The localization has just emerged at the soil surface approximately 1.5 m to the left of the caisson. The caisson and the moving-block soil seem to translate almost as a rigid body, without any appreciable deformation in the soil.

The increase of the fault offset to $h = 0.7$ m leads to the development of a secondary localization towards the standing block, which is quite similar to the one observed in the free-field. This secondary rupture is not only similar in terms of geometry, but also develops for roughly the same bedrock dislocation. This suggests that, in contrast to the previous case, the presence of the caisson is not substantially altering the propagation paths. Indeed, the interaction of the caisson with the propagating fault rupture leads only to a 1.5 m deviation of the main rupture path towards the standing block (i.e., to the left). Quite interestingly, as revealed by the displacement vectors of Fig. 11b, the caisson rotates anti-clockwise (i.e., opposite to what would be expected). This is due to partial loss of support close to the right edge of its base, exactly because of the interaction with the outcropping fault rupture. With the exception of an additional secondary rupture that makes its appearance to the right of the caisson, further increase of h does not seem to provoke any substantial changes in the interaction mechanism.

As in the previous case, the numerical findings (Fig. 11c) agree fairly well with the experimental results. The analysis captures the diversion of the primary fault rupture towards the standing block (to the left) due to its interaction with the left base corner of the caisson. The secondary rupture is also predicted quite accurately, although there is a discrepancy with respect to the additional steeper secondary rupture that develops in the end (for $h = 1.2$ m), which is not captured in the analysis.

Figure 12 compares experimental versus theoretical results in terms of evolution with bedrock offset h of translation and rotation at the top of the caisson, and vertical displacement profiles at the ground surface. The caisson now follows the moving block, and hence the vertical displacement Δz is substantially larger (Fig. 12a).

However, exactly because the interaction with the outcropping dislocation is not as intense, the horizontal displacement Δx and the rotation θ (Fig. 12b) are much lower. The horizontal displacement of the

Fig. 11 Interaction of the caisson foundation with a normal fault rupture at $s/B = -0.80$. Comparison of experimental with numerical analysis results **a** images of the deformed physical model, and **b** displacement vectors computed through image analysis; compared to **c** 3D FE deformed mesh with superimposed plastic strain contours

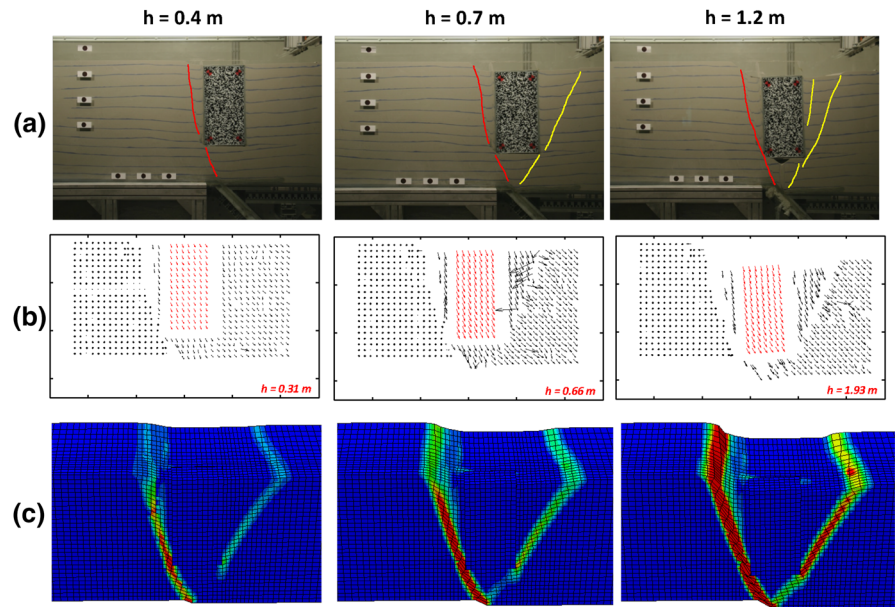
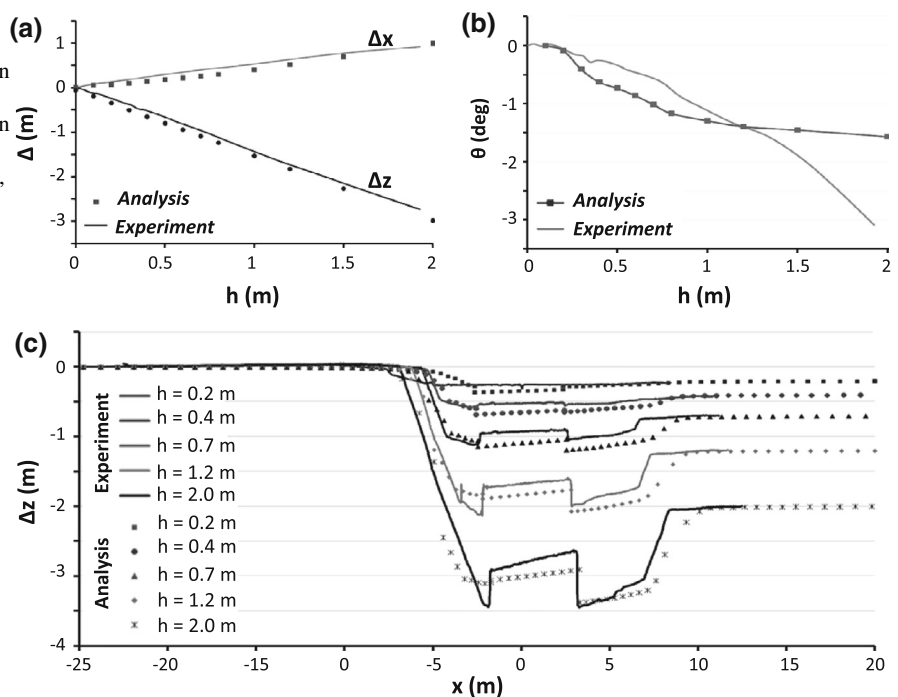


Fig. 12 Interaction of the caisson foundation with a normal fault rupture at $s/B = -0.80$. Comparison of experimental with numerical analysis results in terms of evolution with bedrock offset h of **a** vertical Δz and horizontal Δx displacement, **b** rotation at the top of the caisson foundation; and **c** vertical displacement profile at the ground surface

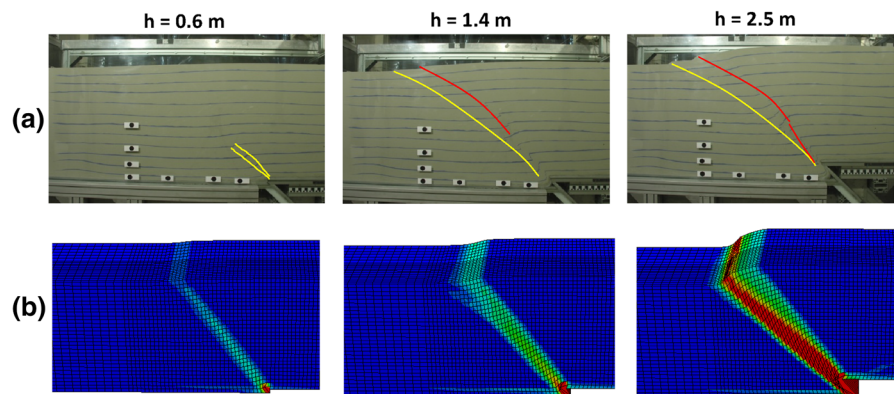


caisson top consists of two components: one being the horizontal translation, and one associated with its rotation. In the previous case, Δx was mainly due to the second component (i.e., the rotation). In this case, the horizontal translation is definitely larger (since it actually moves with the moving block) but the rotation

θ is much lower, so that Δx at the top ends up being much smaller.

The numerical prediction is quite successful in terms of vertical Δz and horizontal displacement Δx (Fig. 12a), but underestimates the rotation θ (Fig. 12b) for $h > 1.2$ m. In terms of vertical

Fig. 13 Reverse fault rupture propagation in the free field. Comparison of **a** images of the deformed physical model, compared to **b** 3D FE analysis deformed mesh with superimposed plastic deformation



displacement profiles at the ground surface the comparison is successful (Fig. 12c).

5 Thrust faulting

As for normal faulting, the free field case is presented first, followed by the interaction of the caisson with the outcropping fault rupture for two characteristic locations.

5.1 Free-field fault rupture propagation

Selected images of the deformed physical model are compared with the 3-dimensional FE deformed mesh and its plastic strain contours in Fig. 13. In the experiment, the fault rupture has only propagated to about a third of the height of the soil deposit for bedrock fault offset $h = 0.6$ m. Although no strain localization (expressed in the form of a fault scarp) can be observed, the quasi-elastic deformation (upheaval) of the ground surface is visible. The analysis is compatible with the experiment, with a relatively low strain shear zone propagating to the soil surface, but not yet developing a distinguishable scarp.

For $h = 1.0$ m (not shown here), the fault rupture outcrops at a distance of about 16 m from the fault initiation point. Further increase of the bedrock fault offset to $h = 1.4$ m leads to the development of a secondary failure plane (yellow line), which outcrops to the left of the primary (i.e., towards the standing block). Further increase of h to 2.5 m simply leads to strain accumulation along the already developed shear zones, which tend to become more distinct.

The numerical analysis predicts a similar failure pattern, but the two distinct failure zones of the

experiment are not discernible. The primary fault rupture reaches the ground surface a little earlier than in the experiment, for $h = 0.8$ m, and a distinct failure plane is fully developed for almost twice that offset ($h = 1.5$ m). The analysis predicts a single broad failure region, the width of which is almost equal to the distance between primary and secondary fault rupture paths in the experiment. In agreement of theoretical, experimental, and field observations [e.g. 28], the failure plane tends to bend over the standing block of the fault: the dip angle decreases.

The above conclusions are further elucidated in Fig. 14, which compares the vertical displacement profile of the ground surface for five values of bedrock fault offset. The two distinct fault scarps of the experiment, are conspicuous: the first one at -15 m and the second one at about -3 m. As previously discussed, the response gets complicated by scale effects. At the beginning, a very large friction angle is mobilized due to the small stress levels. In contrast to normal faulting, the soil is being compressed rather than extended. Hence, progressively, the mobilized friction angle decreases, leading to reduced “bending” of the rupture path over the standing block, i.e. to a steeper failure zone. The numerical analysis cannot fully capture such complicated response, predicting a single much wider dislocation, positioned between the two fault zones of the experiment.

5.2 Interaction of the Caisson with a thrust fault

5.2.1 $s/B = 0.66$

In this test, the caisson foundation was positioned so that the unperturbed (free field) fault rupture would

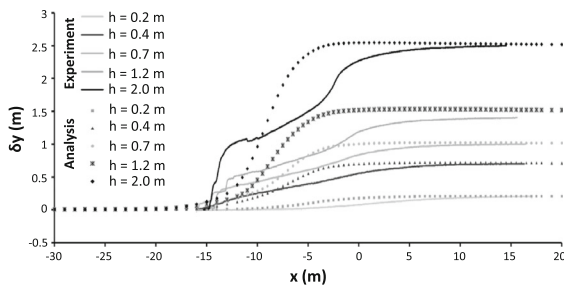


Fig. 14 Reverse fault rupture propagation in the free field. Comparison between numerical analysis and experiment in terms of vertical displacement profile at the ground surface for characteristic values of imposed bedrock offset h

have crossed the caisson base close to its middle. Figure 15 compares experimental images and displacement vectors with FE deformed mesh and plastic strain contours. Forced by the caisson, the fault rupture deviates more than 8 m towards the left edge of its base, progressively becoming less steep as it propagates to the surface. As also revealed by the displacement vectors, although strain localization starts early (for $h < 1$ m), the fault trace clearly outcrops only after $h = 1.4$ m. A secondary rupture plane can also be noticed, starting from the bedrock fault initiation point and reaching the right edge of the caisson at its base. As a result, a triangular wedge is formed underneath the caisson base. A more diffuse shear zone develops along the right wall of the caisson. In other words, the caisson acting as a kinematic constraint leads to bifurcation of the fault rupture, with one branch being diverted towards the standing block, and the other “grazing” the right wall of the caisson.

The incremental displacement vectors of Fig. 15b suggest that the two failure branches develop concurrently. The failure mechanisms (identified by the discontinuities of incremental displacements) are in agreement in general with the above image observations and are highlighted with blue dotted lines. The numerical analysis predicts exactly the same failure mechanism, with the fault rupture bifurcating. The effectiveness of the analysis is further elucidated in Fig. 16, which compares the results in terms of evolution with h of the translation and rotation at the top of the caisson, and of the vertical displacement profiles of the surface. The analysis captures accurately the translation of the caisson, overestimating the rotation by 35 %, on the average. The analysis

compares adequately well with the experiment in terms of vertical displacement profile (Fig. 16c).

5.2.2 $s/B = -0.04$

In this second reverse fault test, the caisson was positioned further to the left (i.e., towards the standing block) so that the unperturbed free field rupture would have interacted with its right wall near the lower corner. Selected experimental images and displacement vectors are compared with the FE deformed mesh and plastic strains in Fig. 17.

For $h = 0.7$ m the fault rupture upon reaching the base of the caisson splits in several fault branches, being in essence diffused. The caisson resists the imposed deformation, and none of these fault branches emerges on the surface even when $h > 2.0$ m. The only observed surface dislocation develops at the right wall of the caisson—the result of sliding at the soil–foundation interface. A complex failure mechanism develops, combining shear straining along the main rupture path and bearing capacity failure at the left wall of the caisson due to its counterclockwise rotation. The increase of bedrock offset to 1.5 m and finally to 2.0 m leads to new bifurcations. Due to the intense interaction between the caisson and the soil, each developing failure mechanism soon becomes kinematically inadmissible, leading to the development of another, and so on.

The numerical analysis is in qualitative agreement with the experiment, but not all of the aforementioned failure mechanisms could be reproduced in detail. Scale effects are partly to blame. The FE model cannot fully replicate such (perhaps spurious) phenomena, leading to a much simpler and perhaps not less realistic response. The same conclusions can be drawn from Fig. 18, which compares the numerical prediction with the experimental results in terms of vertical displacement profile at the ground surface.

6 Summary and conclusions

The paper has presented an experimental and theoretical study focusing on the effects of two types of *dip-slip* faulting on massive caisson foundations. Whether normal or thrust, a fault rupture (i.e., a “shear band”) propagating into the soil interacts with the rigid caisson foundation producing new failure mechanisms,

Fig. 15 Interaction of the caisson foundation with a reverse fault rupture at $s/B = -0.66$. Comparison of experimental with numerical analysis results **a** images of the deformed physical model, and **b** displacement vectors computed through image analysis; compared to **c** 3D FE deformed mesh with superimposed plastic strain contours

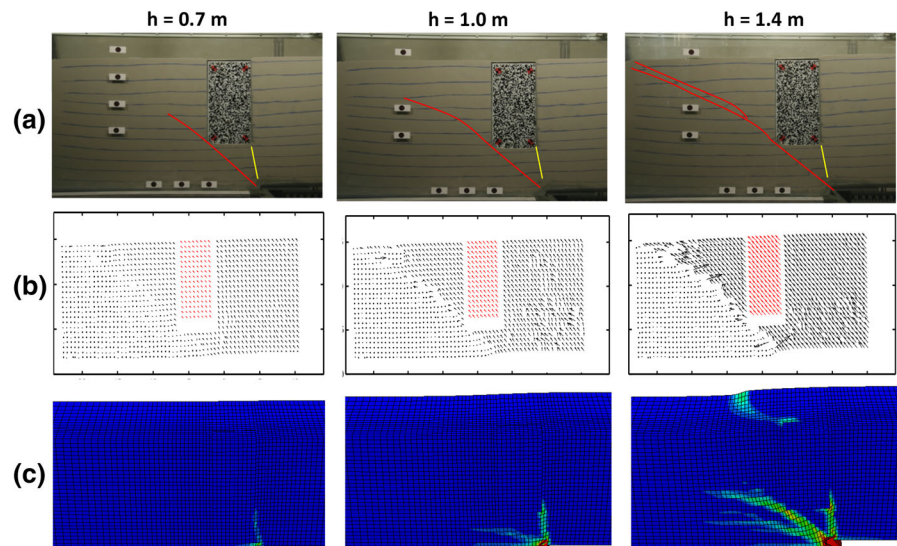
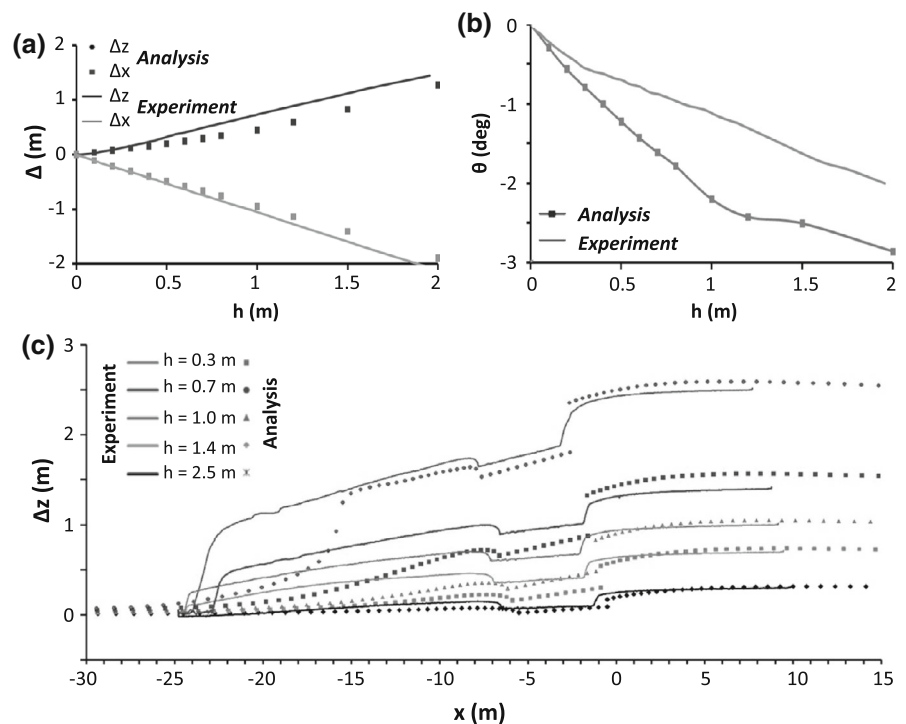


Fig. 16 Interaction of the caisson foundation with a reverse fault rupture at $s/B = -0.66$. Comparison of experimental with numerical analysis results in terms of evolution with bedrock offset h of **a** vertical Δz and horizontal Δx displacement, **b** rotation θ at the top of the caisson foundation; and **c** vertical displacement profile at the ground surface



including diversion, bifurcation, and diffusion of the shear band. The developing failure mechanisms are shown to depend profoundly on the faulting type, the exact location of the foundation relative to the fault, and the magnitude of the fault offset. The developed reasonably sophisticated numerical methodology is validated against the experimental results, although it

cannot always capture the detailed strain localizations observed in the experiments. It is noted that some of these discrepancies between numerical and experimental results are largely related to the unavoidable small-scale effects. Nevertheless, the predicted translational and rotational movements of the top of the caisson are in accord with the experiments.

Fig. 17 Interaction of the caisson foundation with a reverse fault rupture at $s/B = -0.04$. Comparison of experimental with numerical analysis results **a** images of the deformed physical model, and **b** displacement vectors computed through image analysis; compared to **c** 3D FE deformed mesh with superimposed plastic strain contours

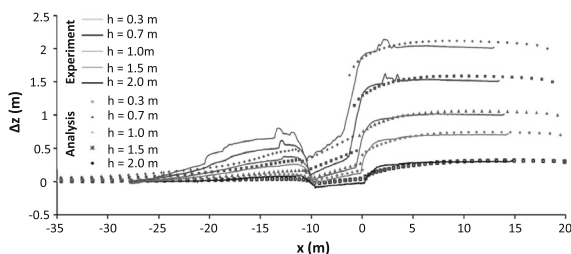
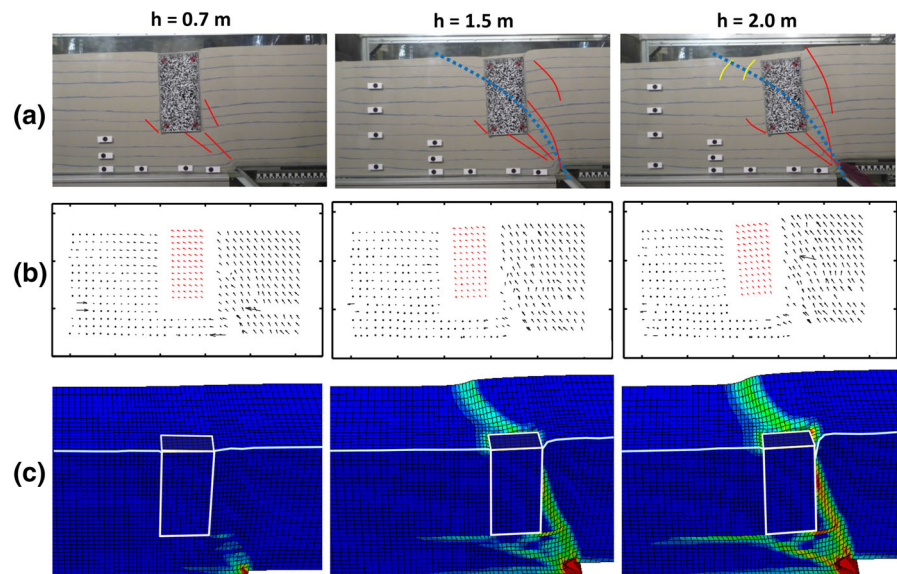


Fig. 18 Interaction of the caisson foundation with a reverse fault rupture at $s/B = -0.04$. Comparison of experimental with numerical analysis results in terms of evolution with bedrock offset h of the vertical displacement profile at the ground surface

Acknowledgments This work formed part of the research project SERIES: “Seismic Engineering Research Infrastructures for European Synergies” (www.series.upatras.gr), which is funded through the Seventh Framework Programme of the European Commission FP7/2007–2013, supported under Grant Agreement No. 227887 of the Research Infrastructures Programme.

References

- Oettle NK, Bray JD (2013) Geotechnical mitigation strategies for earthquake surface fault rupture. *Geotechn Eng* 139(11):1864–1874
- Chang K-C, Chang D-W, Tsai M-H, Sung Y-C (2000) Seismic performance of highway bridges. *Earthq Eng Eng Seism* 2(1):55–77
- Youd TL, Bardet JP, Bray JD (2000) Kocaeli, Turkey, Earthquake of August 17, 1999 Reconnaissance Report. *Earthq Spectra Suppl. A* to 16:456
- Kawashima K (2001) Damage of bridges resulting from fault rupture in the 1999 Kocaeli and Düzce, Turkey earthquakes and the 1999 Chi-chi, Taiwan earthquake. Workshop on seismic fault-induced failures: Possible remedies for damage to urban facilities, University of Tokyo, Tokyo, 171–190
- Pamuk A, Kalkan E, Ling HI (2005) Structural and geotechnical impacts of surface rupture on highway structures during recent earthquakes in Turkey. *Soil Dyn Earthq Eng* 25(7–10):581–589
- Faccioli E, Anastasopoulos I, Calliero A, Gazetas G (2008) Case histories of fault–foundation interaction. *Bull Earthq Eng* 6:557–583
- Anastasopoulos I, Gazetas G (2007) Foundation–structure systems over a rupturing normal fault: Part I. Observations after the Kocaeli 1999 earthquake. *Bull Earthq Eng* 5(3): 253–275
- Anastasopoulos I, Gazetas G (2007) Behaviour of structure–foundation systems over a rupturing normal fault: Part II. Analysis of the Kocaeli Case Histories. *Bull Earthq Eng* 5(3):277–301
- Liu Q, Li X (2009) Preliminary analysis of the hanging wall effect and velocity pulse of the 5.12 Wenchuan earthquake. *Earthq Eng Eng Vib* 8(2):165–178
- Wang Z, Lee CG (2009) A comparative study of bridge damage due to the Wenchuan, Northridge, Loma Prieta and San Fernando earthquakes. *Earthq Eng Eng Vib* 8(2): 251–262
- Bray JD, Seed RB, Cluff LS, Seed HB (1994) Analysis of earthquake fault rupture propagation through cohesive soil. *J Geotech Eng* 120(3):562–580
- Paolucci R, Yilmaz MT (2008) Simplified theoretical approaches to earthquake fault rupture–shallow foundation interaction. *Bull Earthq Eng* 6(4):629–644
- Anastasopoulos I, Gazetas G, Drosos V, Georgarakos T, Kourkoulis R (2008) Design of bridges against large tectonic deformation. *Earthq Eng Eng Vib* 7:345–368

14. Anastasopoulos I, Gazetas G, Bransby MF, Davies MCR, El Nahas A (2009) Normal fault rupture interaction with strip foundations. *J Geotech Geoenviron Eng ASCE* 135(3):359–370
15. Loli M, Anastasopoulos I, Bransby MF, Waqas A, Gazetas G (2011) Caisson foundations subjected to reverse fault rupture: centrifuge testing and numerical analysis. *J Geotechn Geoenviron Eng ASCE* 137(10):914–925
16. Bray JD (2001) Developing mitigation measures for the hazards associated with earthquake surface fault rupture, A Workshop on Seismic fault-induced failures—Possible Remedies for Damage to Urban Facilities, Japan Society for the Promotion of Sciences, 55–79
17. Bray JD (2009) Designing buildings to accommodate earthquake surface fault rupture, improving the seismic performance of existing and other structures. ASCE, Reston, pp 1269–1280
18. Fadaee M, Anastasopoulos I, Gazetas G, Jafari MK, Kamalian M (2013) Soil bentonite wall protects foundation from thrust faulting: analyses and experiment. *Earthq Eng Eng Vib* 12(3):473–486
19. Gazetas G, Pecker A, Faccioli E, Paolucci R, Anastasopoulos I (2008) Design recommendations for fault–foundation interaction. *Bull Earthq Eng* 6(4):677–687
20. Cole DA Jr, Lade PV (1984) Influence zones in alluvium over dip-slip faults. *J Geotech Eng* 110(5):599–615
21. Trautmann CH, O'Rourke TD (1985) Lateral force displacement response of buried pipe. *Journal of Geotechnical Engineering ASCE* 111(9):1077–1092
22. O'Rourke TD, Jezerski JM, Olson NA, Bonneau AL, Palmer MC, Stewart HE, O'Rourke MJ, Abdoun T (2008) Geotechnics of pipeline system response to earthquakes. *Geotechn Earthq Eng Soil Dyn GSP* 181, ASCE
23. Abdoun TH, Ha D, O'Rourke MJ, Symans MD, O'Rourke TD, Palmer MC, Stewart HE (2009) Factors influencing the behavior of buried pipelines subjected to earthquake faulting. *Soil Dyn Earthq Eng* 29(3):415–427
24. Muir Wood D (2004) *Geotechnical modelling*. Spon Press, London and New York
25. Anastasopoulos I, Georgarakos T, Georgiannou V, Drosos V, Kourkoulis R (2010) Seismic performance of bar-mat reinforced-soil retaining wall: shaking table testing versus numerical analysis with modified kinematic hardening constitutive model. *Soil Dyn Earthq Eng* 30(10):1089–1105
26. Bolton MD (1986) The strength and dilatancy of sands. *Geotechnique* 36(1):65–78
27. White DJ, Take WA, Bolton MD (2003) Soil deformation measurement using particle image velocimetry (PIV) and photogrammetry. *Geotechnique* 53(7):619–631
28. Bray JD, Seed RB, Cluff LS, Seed HB (1994) Earthquake fault rupture propagation through soil. *J Geotech Eng* 120(3):543–561
29. Anastasopoulos I, Gazetas G, Bransby MF, Davies MCR, El Nahas A (2007) Fault rupture propagation through sand: finite element analysis and validation through centrifuge experiments. *J Geotech Geoenviron Eng ASCE* 133(8):943–958
30. Loukidis D, Bouckovalas G, Papadimitriou AG (2009) Analysis of fault rupture propagation through uniform soil cover. *Soil Dyn Earthq Eng* 29(11–12):1389–1404
31. Bransby MF, Davies MCR, El Nahas A, Nagaoka S (2008) Centrifuge modelling of normal fault–foundation interaction. *Bull Earthq Eng* 6(4):585–605